

Constitutive Behavior and Processing Maps of a New Wrought Magnesium Alloy ZE20 (Mg-2Zn-0.2Ce)

Scott Sutton^{a,1}, and Alan A. Luo^{a, b,2}

^aDepartment of Materials Science and Engineering, The Ohio State University, Columbus, OH 43210, USA

^bDepartment of Integrated Systems Engineering, The Ohio State University, Columbus, OH 43210, USA

Abstract

ZE20 (Mg-2Zn-0.2Ce)³ is a new wrought magnesium alloy with improved extrudability and mechanical properties [1]. To understand the constitutive behavior and workability of this new alloy, Gleeble thermomechanical testing has been carried out in this study. The flow stress behavior of ZE20 was investigated between 250°C to 450°C and 10⁻³ s⁻¹ to 1.0 s⁻¹ in isothermal compression. Constitutive descriptions of the flow stress are provided. A new general approach at application of the extended Ludwik equation is demonstrated and was found to be more accurate than the hyperbolic sine Arrhenius model while having a similar number of model constants. Processing maps were developed based on the experimental results and are verified with microstructural investigation. A region of safe processing with non-basal texture and high activity of dynamic recrystallization (DRX) was found between 375°C and 450°C, from 10⁻¹ s⁻¹ to 10^{-2.5} s⁻¹. A region of potentially safe processing with annealing that is associated with shear band nucleation of non-basal grains was identified for temperatures as low as 300°C and rates as high as 10⁻¹ s⁻¹.

Keywords: magnesium alloys, thermomechanical processing, constitutive behavior, processing map, deformation mechanisms.

¹ Present affiliation: Mag Specialties Inc., Denver, CO 80210, USA

² Corresponding author. Tel.: +1 6142925629. Email: luo.445@osu.edu

³ All compositions in wt.% except otherwise stated.

1. Introduction

Lightweighting is an increasingly effective approach to improving vehicle fuel efficiency and reducing greenhouse gas emissions in the automotive industry. Given that Mg has the lowest density of any structural metal, it is an attractive choice for vehicle lightweighting. Though die casting presents the most efficient manufacturing process for implementing Mg in automotive applications, both in terms of productivity and potential part consolidation [2,3], wrought Mg components have successfully replaced some non-critical structures in automotive design [3]. Magnesium sheet and extrusions have received increasing attention from the automotive industry, but wrought Mg still faces several barriers to widespread application. Chief among these barriers are magnesium's low formability at room temperature, and its tendency to form strong basal deformation textures. Both of these can be related to magnesium's crystal structure and deformation mechanisms.

Being hexagonal close packed with a c/a ratio less than the ideal value, Mg has few easy deformation modes. The most important slip systems in Mg include $(0002)\langle 10\bar{1}0 \rangle$ slip, $\{10\bar{1}0\}\langle 11\bar{2}0 \rangle$ slip, $\{10\bar{1}\bar{1}\}\langle 11\bar{2}0 \rangle$ slip, and $\{10\bar{1}\bar{1}\}\langle 11\bar{2}\bar{3} \rangle$ slip, also referred to as basal slip, prismatic slip, pyramidal $\langle a \rangle$ slip, and pyramidal $\langle c+a \rangle$ slip, respectively [4,5]. Though the specific values of critical resolved shear stress (CRSS) for each of these slip systems depend on alloy composition [2], basal slip is recognized as having the lowest CRSS of these deformation modes at room temperature. Magnesium also possesses several twinning modes, of which the most relevant for plasticity are $\{10\bar{1}\bar{2}\}\langle 10\bar{1}\bar{1} \rangle$ twinning and $\{10\bar{1}\bar{1}\}\langle 10\bar{1}\bar{2} \rangle$ twinning, or "tension twinning" and "compression twinning", respectively [6,7]. Tension twinning has a CRSS on par with that of basal slip and imparts limited ability for the crystal to accommodate strain along its c -axis. Compression twinning has a very high CRSS and is seldom activated; as such, it is often excluded from consideration in plasticity simulations [8]. It is noteworthy that if compression twinning does occur, it rotates material into an orientation very favorable for deformation, leading to strain localization and failure [7].

Despite the number and complexity of deformation modes in Mg, it is easy to show a simplified view of monotonic compression for Mg polycrystals. Under applied strain, basal slip and tension twinning will operate in tandem at low stresses; twinning contributes greatly to basal texture formation and orientation hardening at low strains [6]. Possessing higher CRSS, prismatic and pyramidal $\langle a \rangle$ slip is activated at moderate stress [9], though it does not accommodate much strain in the now basal-textured polycrystal. With further strain, either the material fails, or pyramidal $\langle c+a \rangle$ slip activates at high stress, providing strain accommodation until ultimate fracture. Because pyramidal $\langle c+a \rangle$ slip is the only slip system to provide strain accommodation along the unit cell's $\langle c \rangle$ axis (approximately along a basal textured polycrystal's compression axis) [9], it is a key slip system for process and design considerations. In addition to prismatic and pyramidal $\langle a \rangle$ slip, pyramidal $\langle c+a \rangle$ slip's CRSS can be lowered by increasing the deformation temperature [8]. The CRSS of any slip mode can be sensitive to alloying as well, and the elements which soften non-basal slip or harden basal slip relative to non-basal slip are considered favorable alloying elements [10,11].

From a processing standpoint, the easy texture formation in Mg at even low stress and strain is problematic. For most wrought products, the dominant stress state is compressive, leading to a strong texture where basal planes are aligned perpendicular to the compression axis [12,13]. Such basal texture gives sheet and extrudates macroscopic anisotropy and tension-compression yield asymmetry [14], resulting in limited subsequent formability. The traditional approach to mitigate the effects of texture is by heating Mg components during secondary forming operations, thereby thermally activating non-basal slip modes. Unfortunately, this is not always practical, as heating and annealing schedules come with an associated cost. Currently, two other main strategies exist to overcome the barriers imposed by magnesium's mechanical behavior: grain refinement and texture modification [15]. Texture modification strategies aim to reduce the intensity of basal texture, consequently mitigating anisotropy and yield asymmetry and increasing formability. Grain refinement aims to obviate the need for texture control, as studies have shown that twinning is suppressed in very fine grained Mg [16,17], resulting in increased ductility and reduced tension-compression asymmetry [18]. Refined microstructures can be produced by severe plastic deformation (SPD) processing, such as equal channel angular processing (ECAP) [19] or high pressure torsion [20]. Fine grained Mg can also be produced using small alloying additions of Zr, as in the case of Mg alloys ZK60 and ZEK100.

In the most widely used wrought Mg alloy, AZ31 (Mg-3Al-1Zn), various aspects of plastic deformation, forming, processing, texture, and recrystallization have been extensively studied [4,5,8,16,21-28]. With the ever-increasing industrial demand of lightweight materials, new emphasis has been placed on alloy development and the search for higher performing Mg alloys. The current generation of rare-earth-containing Mg alloys achieves both texture modification and grain refinement to some extent via enhanced recrystallization [29,30]. While conventional Mg alloys tend to retain the parent material's basal texture through recrystallization [31], the addition of rare earths can help nucleate new grains in non-basal orientations either through particle-stimulated nucleation (PSN) [14,32] or through shear band nucleation (SBN) [33]. After nucleation, rare earths have been shown to slow growth of new grains, either through particle pinning effects [34] or through strong interaction of solutes with dislocations and grain boundaries [35]. Strong

solute-dislocation interaction is also an accepted cause of dynamic strain aging (DSA), and processing under conditions where DSA is expected to occur has been shown to influence the formation of non-basal texture [36].

ZE20 (Mg-2Zn-0.2Ce), patented by Luo et al., is one of the most viable alloys of the current generation in terms of its superior formability and low cost [37]. It combines the texture reduction and recrystallization properties imparted by Ce additions [34] with solid solution strengthening from zinc, resulting in a high ductility, low cost alloy with strength comparable to that of AZ31 [1]. The mechanical behavior of this alloy still has not been adequately described in the literature. Gao and Luo applied the Sellars-Tegart relation to the peak stress of ZE20 but only published select mechanical data and do not model the full flow stress behavior [38]. Bingöl and Misiolek applied artificial neural network (ANN) and gene expression programming (GEP) methods to the low-strain behavior of ZE20, making contradictory and dubious predictions [39]. The present study seeks to provide a complete constitutive description of flow stress in industrially-relevant conditions. A novel formulation of a classical strain hardening model is presented and compared to the Sellars-Tegart model. Processing maps are constructed and used to guide microstructural characterization of mechanisms occurring in different domains of material behavior.

2. Materials and Experimental Methods

The materials used in this study were direct chill cast ZE20 billets, provided in previous work [40] by the United States Automotive Materials Partnership (a consortium of General Motors, Ford and Fiat Chrysler). Alloy chemistry was verified via optical emission spectroscopy and is shown in Table 1.

Table 1
Chemical composition of ZE20 alloy

Element	Ce	Mn	Zn	Th	Si	Trace others (<0.01% each)	Mg
Composition (wt. %)	0.2686	0.3599	1.966	0.1213	0.01086	0.02863	Balance

Compression cylinders of 15mm length and 10mm diameter were machined from the as-cast billets via electrical discharge machining (EDM). Uniaxial compression testing was performed at constant true strain rates and temperatures using a Gleeble 3800 servo-hydraulic thermomechanical testing system. Specimens were compressed to a true strain⁴ of 1.0 at each combination of temperature and strain rate using strain rate decades from 10^{-3} s^{-1} to 1.0 s^{-1} and temperatures from 250°C to 450°C in 50°C increments. Strain was calculated using the Gleeble's hydraulic ram displacement. Displacement was measured with an internal LVDT having 0.002mm resolution and $\pm 0.25\%$ full scale accuracy over $\pm 2.5\text{mm}$ of travel. Final displacement was verified ex-situ to be within +0.5% to +1.0% of the desired displacement increment. Stress was calculated using the traditional assumption of constant volume of a right cylinder. Force was measured using a load cell with having $\pm 1\text{kg}$ resolution and $\pm 1\%$ full scale accuracy for +10,000/-20,000kg full range. Testing temperature was monitored and maintained constant via K-type thermocouple probes percussion welded directly to the specimen's surface. All specimen temperatures were within $\pm 3^\circ\text{C}$ of the desired testing temperature for the entire duration of the mechanical test. Specimen-platen contact area was well lubricated with 0.005" graphite foil. In order to avoid post-dynamic recrystallization, specimens were water-quenched immediately after testing. Qualitatively, post-test specimens showed very little barreling (if any), but the surface quality of tested specimens prevented accurate measurement of barreling. Mechanical data were not corrected for barreling or adiabatic heating.

Specimens were sectioned axially and polished down to 1 μm diamond abrasive using standard metallographic techniques. Final polish was accomplished using colloidal silica for three minutes. Specimens were etched for 5-8 seconds in a diluted acetic-picric solution consisting of 4.2g picric acid, 10ml acetic acid, 110ml ethanol, and 10ml distilled water. Etched specimens were studied with optical microscopy, and salient microstructural features were examined in detail with scanning electron microscopy (SEM), and electron backscatter diffraction (EBSD).

All electron microscopy was performed on a FEI XL-30 microscope operating at 20 kV. Scan area and step size were varied as appropriate for the features of interest in each scan. Step size was chosen such that there were at least five scan points across the diameter of fine recrystallized grains or other features of interest. Analysis of EBSD data was performed using EDAX OIM software. A light cleanup was used on all datasets. Except where stated, all points with a confidence index of 0.1 were first excluded from the dataset. A single iteration of grain dilation (grain tolerance of 5° , minimum

⁴ All listed strains in the present work are compressive. For simplicity, the negative sign is omitted.

grain size of 5 scan points) followed by neighbor orientation correlation (level 1 cleanup, grain tolerance angle of 5°, minimum confidence index of 0.1) was then applied to the data. Less than 0.5% of the total data set was changed in either cleanup step. EBSD data were partitioned according to grain size. Partitioned datasets were characterized qualitatively with visual inspection, and partitioned textures were analyzed quantitatively using inverse pole figures (IPFs).

3. Numerical Methods

3.1 Hyperbolic Sine Arrhenius model

Despite its empirical nature, the hyperbolic sine Arrhenius type equation proposed by Sellars and McTegart is perhaps the most common constitutive description of flow stress available in the literature [41]. It takes the form

$$\dot{\epsilon} = A [\sinh(a\sigma)]^n \exp\left(\frac{-Q}{RT}\right) \quad (1)$$

where σ , $\dot{\epsilon}$, T , and Q are flow stress, strain rate, absolute temperature, and activation energy of deformation, respectively; and A , a , and n are material constants; and R is the universal gas constant. The Sellars-Tegart relation provides an empirical link across different regimes of material behavior.

At low stresses (at high temperature or low strain rate), Eq. (1) reduces to a power law ($\dot{\epsilon} = A \cdot \sigma^n$) often used to describe creep stresses; and, at high stresses (low temperature or high strain rate), it reduces to an exponential relation ($\dot{\epsilon} = A \cdot \exp(\beta\sigma)$) which is useful for hot working [41]. Knowing all other variables, the Arrhenius portion of the Sellars-Tegart relation allows for determination of activation energy and correlation to the rate-limiting deformation mechanism (diffusion, recovery, or recrystallization at steady state) [42]. These all contribute to the robustness of the model, giving it a very wide range of applicability over a large temperature range and several strain rate decades.

Strain does not enter the Sellars-Tegart relation, and its original intent is to be used with steady state stress [42]. Despite this, many works iteratively apply the Arrhenius equation to all experimental strains [43,44] and achieve satisfactory results for some predictive purposes. With such application, the model constants become functions of strain instead of scalars. The resulting form lends itself to easy reporting, where model constants are typically reported as polynomial functions of strain. Some works argue that this method makes some of the model constants difficult to interpret or lose physical meaning [45]. Other authors note that the only model constant with true physical meaning is the activation energy of deformation, Q [46].

Several sources [44,47,48] in the literature describe the graphical methods used to determine the model constants. Experimental data at every 1% of plastic strain were implemented in the model. The predictive accuracy of the model was evaluated for flow stress at all strains, strain rates, and temperatures using average absolute relative error (AARE) and root mean square error (RMSE), which are defined as

$$error_{AARE} = \frac{1}{N} \sum_{i=1}^N \left| \frac{\sigma_{calculated}^i - \sigma_{experimental}^i}{\sigma_{experimental}^i} \right| \quad (2)$$

$$error_{RMSE} = \sqrt{\frac{1}{N} \sum_{i=1}^N (\sigma_{experimental}^i - \sigma_{calculated}^i)^2} \quad (3)$$

where N is the total number of data points, and i represents the i -th data point.

3.2 Extended Ludwik Strain Hardening

The extended Ludwik equation [49,50] adds strain rate effects to the Hollomon equation via an additional power term. It takes the form

$$\sigma = K \epsilon_p^n \left(\frac{\dot{\epsilon}}{\dot{\epsilon}_0}\right)^m \quad (4)$$

where K is the strength coefficient, ϵ_p is effective plastic strain, n is the strain hardening rate, and m is the strain rate sensitivity. In this form, $\dot{\epsilon}_0$ is a reference strain rate (usually taken to be 1 s⁻¹) so that no dimensional terms are involved in the power law. When using the extended Ludwik equation to model strain hardening over a range of temperatures, K , n , and m are taken to be functions of temperature and independent of strain or strain rate [49]. This formulation of the extended Ludwik equation has been used successfully to model the flow stress of cast aluminum at low strains [44,51],

but it would poorly capture the behavior of ZE20 at high strains. At a given temperature, n is single-valued in Eq. (4) and cannot capture both low strain work hardening and high strain softening due to DRX.

Changes in hardening behavior can be modeled using multiple-stage strain hardening, similar to the “double- n effect” reported in iron and steels [52], where the strain hardening exponent and strength coefficient change values after some critical strain. Unfortunately, the hardening behavior of ZE20 is not well-described by a simple two-stage or multiple stage linear strain hardening exponent. In the present work, we instead express the strain hardening rate as a continuous function of strain while also incorporating strain rate and temperature dependence.

Determination of constants for the traditional version extended Ludwik equation is straightforward. Taking the natural logarithm of Eq. (4) results in

$$\ln \sigma = \ln K + n \ln \varepsilon + m \ln \dot{\varepsilon} \quad (5)$$

Taking the partial derivative with respect to strain rate gives

$$m = \left[\frac{d \ln \sigma}{d \ln \dot{\varepsilon}} \right]_T \quad (6)$$

Equation (5) can be used to find m and K simultaneously via graphical methods. On a plot of $\ln(\sigma)$ as a function of $\ln(\varepsilon)$, m is the slope of the plot, and $\ln(K)$ is the intercept. Average values of m and K are taken across all strain rates. For ease of reporting, polynomial fits of $m(T)$ and $K(T)$ are used. The strain hardening rate is determined by taking the partial derivative of Eq. (5) with respect to strain. For the traditional model, it takes a form similar to Eq. (6):

$$n = \left[\frac{d \ln \sigma}{d \ln \varepsilon} \right]_T \quad (7)$$

To instead obtain a strain hardening function, n' , which varies with strain, we differentiate Eq. (5) using the chain rule:

$$\frac{d \ln(\sigma)}{d \varepsilon} = \frac{dn'}{d \varepsilon} \ln(\varepsilon) + \frac{n'}{\varepsilon} \quad (8)$$

For the temperatures and strain rates used in the present study, the left hand side of the equation is well described by an exponential function. Substituting an exponential function with arbitrary constants into Eq. (8) gives

$$\frac{dn'}{d \varepsilon} \ln(\varepsilon) + \frac{n'}{\varepsilon} = A \exp(B \varepsilon) + C \quad (9)$$

Solving the differential equation results in

$$n' = \frac{1}{\ln(\varepsilon)} \left[\frac{A}{B} \exp(B \varepsilon) + C \varepsilon + D \right] \quad (10)$$

where A , B , C , and D are functions of strain rate and temperature. The overall expression for flow stress is obtained by substituting Eq. (10) into Eq. (4):

$$\sigma = K \left(\varepsilon^{\left\{ \frac{1}{\ln(\varepsilon)} \left[\frac{A}{B} \exp(B \varepsilon) + C \varepsilon + D \right] \right\}} \right) \left(\frac{\dot{\varepsilon}}{\dot{\varepsilon}_0} \right)^m \quad (11)$$

The constants A , B , C , and D were evaluated at each combination of temperature and strain rate, and a second-order polynomial surface was fit to the each constant (A , B , C , and D) in $\ln(\varepsilon)$ - T space. As with the Arrhenius model, the accuracy of the extended Ludwik model was evaluated with AARE and RMSE (Eq. (2) and Eq. (3)). Because polynomial surfaces are sensitive to the values of the points used, especially because they incorporate a $\ln(\varepsilon)$ axis, a light optimization was applied to the coefficients of A , B , C , and D (no optimization was performed for m or K). An iterative gradient descent method was used, on the basis of minimizing the AARE of the final equation. After optimization, values of n' were verified to remain accurate to actual material behavior for each temperature and strain rate. Results of both the optimized solution and the original solution are compared to the Sellars-Tegart model.

3.3 Processing Maps

Processing maps are a useful tool for hot forming operations which describe the optimal conditions for forming a material at different temperatures, strain rates, and strains. The most commonly used construction of processing maps relate this by superimposing an efficiency term developed by Prasad et al. and an instability criterion subsequently developed by Kumar and Prasad [53–55]. The work by Prasad et al. is based on a variational principle analysis of rigid viscoplastic material behavior by Oh and Lee and Kobayashi [56,57]. Using principles of the Dynamic Materials Model (DMM) outlined by Wellstead, they modeled the workpiece during deformation as a linear dissipator of power [58]. Briefly, their derivation is as follows:

$$P = \bar{\sigma} \dot{\epsilon} = \int_0^{\dot{\epsilon}} \sigma d\dot{\epsilon} + \int_0^{\sigma} \dot{\epsilon} d\sigma \quad (12)$$

where P is the total power dissipated by the workpiece. This is commonly rewritten as

$$P = G + J \quad (13)$$

where G is the “dissipator content” and J is the “dissipator co-content.” Prasad et al. noted that these terms could be conceptualized in terms of irreversible thermodynamics: G describes the power dissipated by plastic work (mostly heat), and J describes the amount of power dissipated by metallurgical processes [53]. Assuming a power law form of stress ($\sigma = k\dot{\epsilon}^m$), the term of interest J can be evaluated

$$J = \int_0^{\sigma} \dot{\epsilon} d\sigma = \frac{\sigma \dot{\epsilon} m}{m+1} \quad (14)$$

The efficiency of power dissipation via metallurgical processes, η , is the instantaneous value of J normalized by the maximum possible value of J , which occurs at $m = 1$.

$$\eta = \frac{J}{J_{max}} = \frac{\frac{\sigma \dot{\epsilon} m}{m+1}}{\frac{\sigma \dot{\epsilon}}{2}} = \frac{2m}{m+1} \quad (15)$$

Kumar and Prasad incorporated work by Ziegler into this framework[54,55,59]. Ziegler noted that stable flow occurs if

$$\frac{dD}{d\dot{\epsilon}} > \frac{D}{\dot{\epsilon}} \quad (16)$$

is satisfied, where $D(\dot{\epsilon})$ is the dissipative function of the material. Since metallurgical stability is of interest, microstructural stability can be determined by substituting J for D . Simplifying the resulting inequality, the final stability criterion is written as

$$\xi(\dot{\epsilon}) = \frac{d \ln\left(\frac{m}{m+1}\right)}{d \ln \dot{\epsilon}} + m > 0 \quad (17)$$

By convention, processing maps using this method plot η at a certain strain in strain rate – temperature space. Any regions where the inequality in Eq. (17) is not satisfied are marked as regions of plastic instability.

It is noteworthy that these derivations are not universally accepted, but they are the most commonly used – both in research publications [60,61] and in standard reference materials [62,63]. However, material workability has been widely researched, and alternate methods for characterizing it are certainly available in the literature. Raj proposed one of the first processing maps by superimposing regions where different mechanisms operate which could lead to material failure [64]. Shortly afterward, Semiatin and Lahoti proposed a criterion to quantify flow localization, working under the assumption that unstable flow occurs whenever flow softening is observed [65,66]. Murty and Rao have criticized the instability criterion in Eq. (17) because of its use of the power law, and have derived their own more general instability parameter [67]. More recently, Poletti et al. have developed their own criterion by avoiding the use of strain rate sensitivity to describe stable flow and have compared with Prasad’s and Murty’s methods [68]. Still other notable works include Montheillet et al. who work with strain energy density rather than power dissipation [69], and Ghosh who provides an alternate derivation based on thermodynamic quantities for D instead of simple substitution of J for D [70].

4. Results and Discussion

4.1 Mechanical Behavior

The general trends of ZE20's mechanical behavior are similar to those of any metal. Both the yield stress and the flow stress at a given strain increase with increasing strain rate and decrease with increasing temperature. Specific attributes of the flow curves are more interesting, as several regimes of material behavior are evident. The experimental flow curves are shown in Fig. 1.

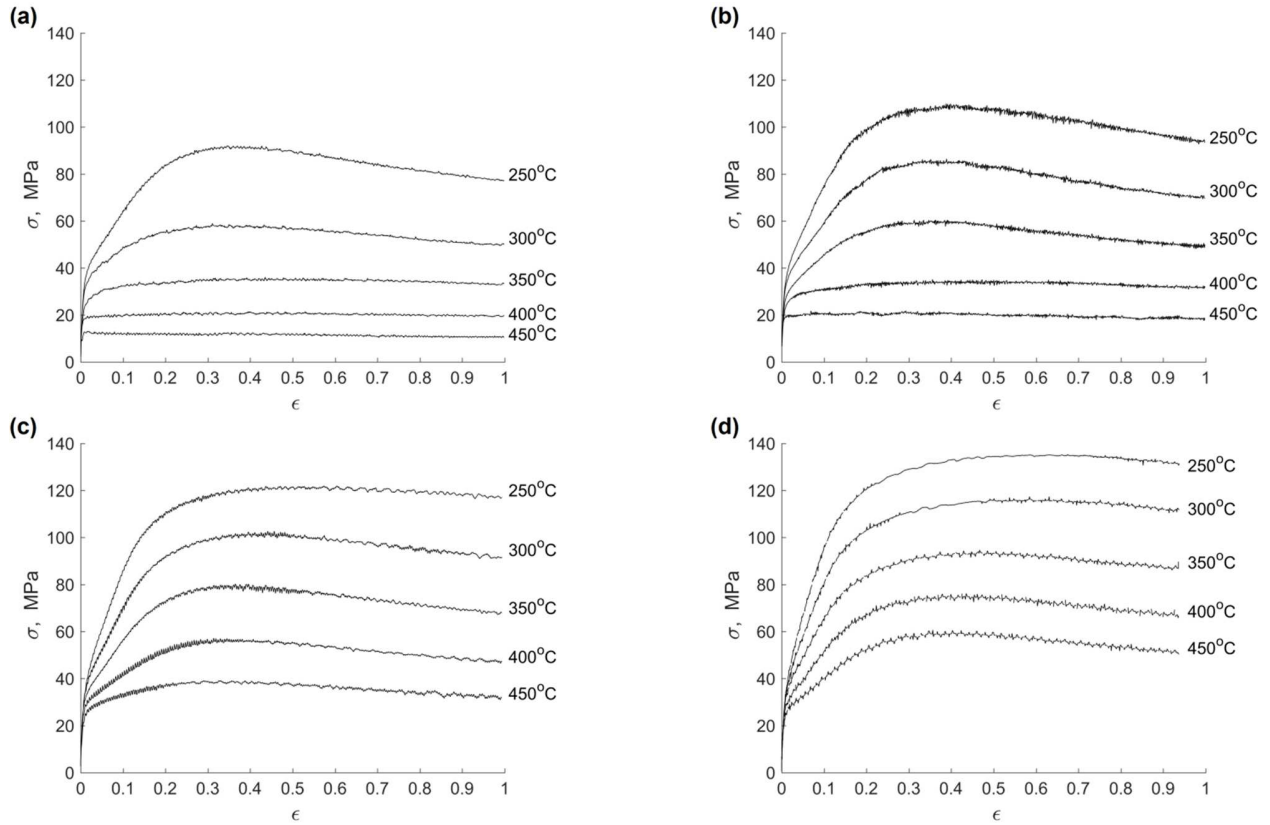


Fig. 1. True stress - true strain curves for ZE20 gathered at (a) 10^{-3} s^{-1} , (b) 10^{-2} s^{-1} , (c) 10^{-1} s^{-1} , and (d) 1.0 s^{-1} .

It is most useful to interpret flow curves on the basis of Zener-Hollomon parameter, Z , as it takes into consideration both temperature and strain rate ($Z = \dot{\epsilon} \cdot \exp(\frac{Q}{RT})$). In regions with low Z (specifically, at 400°C to 450°C and 10^{-2} s^{-1} to 10^{-3} s^{-1} and somewhat at 350°C and 10^{-3} s^{-1}), the flow curves for ZE20 nearly resemble ideal plastic flow; flow stress is nearly constant under these conditions. This is not unreasonable behavior, as 400°C and 450°C translate to high homologous temperatures ($>0.7 T_m$) for Mg, and the applied strain rates are very low. Under these conditions, thermally activated phenomena such as DRX or even creep are not kinetically limited and should govern the material response.

In regions with high Z (specifically, 250°C to 300°C at 10^0 s^{-1} and 250°C and 10^{-1} s^{-1}), flow stress rises to a steady state value, after which little softening is evident. This behavior is classically attributed to dynamic recovery (DRV) in FCC materials with high stacking fault energy, such as Al and Cu; it has also been studied in Mg, though it should operate to a lesser extent [71,72]. DRX should also operate at these strain rates and temperatures, and it should be responsible for the slight softening seen at high strain for these curves. DRX and DRV should operate in tandem to produce the effect seen in the flow curves.

In regions with intermediate Z , the flow curves exhibit yielding followed by linear or concave-down hardening until they reach a peak stress at approximately 20% - 40% strain, followed by significant flow softening. Such behavior is classically attributable to DRX.

4.2 Constitutive Models

Both constitutive models achieved satisfactory results. The experimental data is plotted along with predicted flow curves in Fig. 2 to facilitate qualitative comparison of both models' performance.

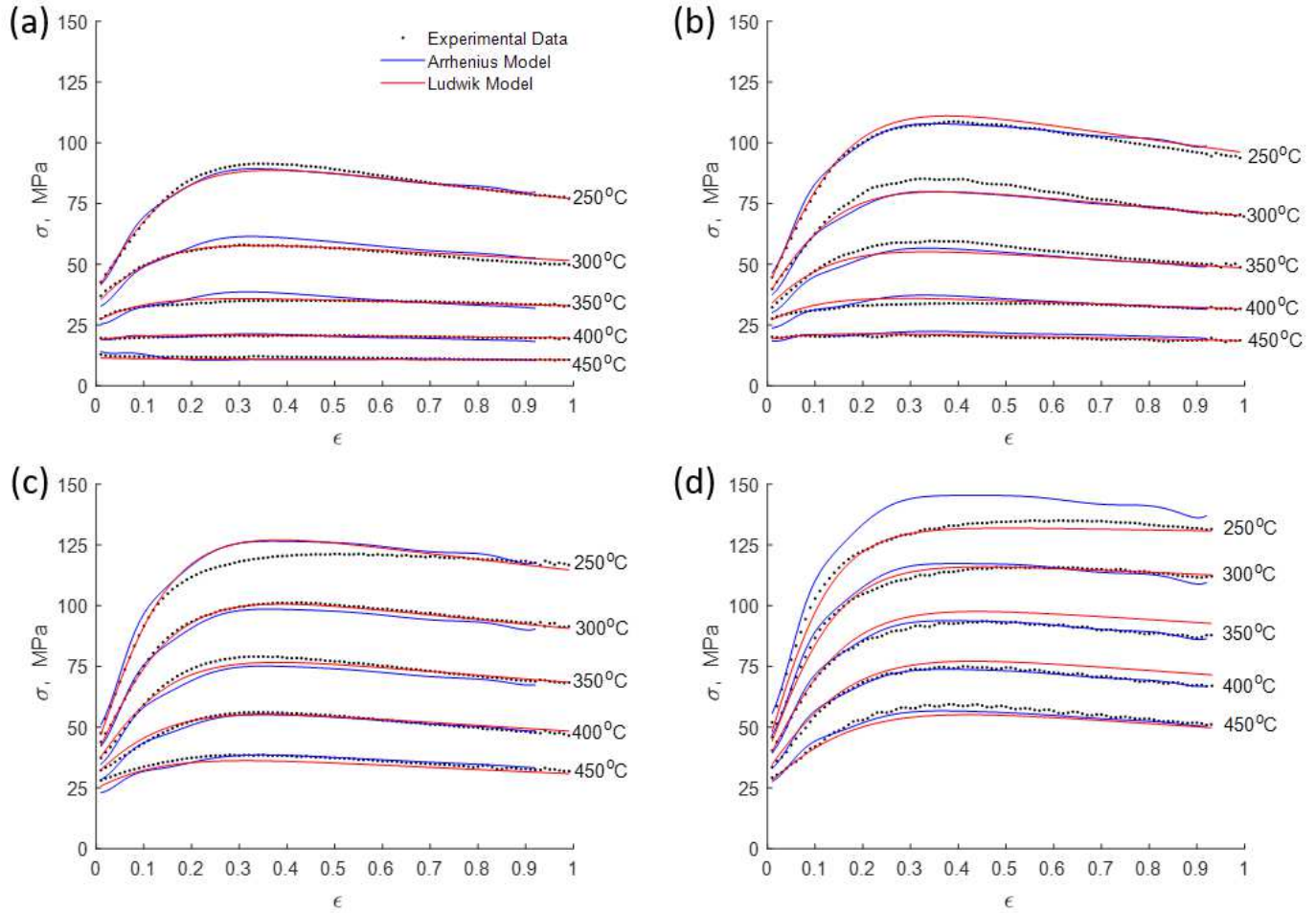


Fig. 2. Comparison of model predictions and experimental flow stress data at (a) 10^{-3} s^{-1} , (b) 10^{-2} s^{-1} , (c) 10^{-1} s^{-1} , and (d) 1.0 s^{-1} . For the Ludwik model, only the optimized solution is shown.

By simple inspection of Fig. 2, both models perform the best at high temperatures and low strain rates. Moving to lower temperatures and higher strain rates, neither model predicts flow stress completely accurately as the material behavior changes to DRV-like behavior. Instead of predicting hardening to high strains and steady state behavior, both models predict a peak stress at about 25% strain followed by work softening at temperatures of 300°C and below and rates of 10^{-1} s^{-1} and above. At 250°C and 1.0 s^{-1} , the Arrhenius model far over-predicts flow stress and is likely outside the model's applicable range.

Overall, the hyperbolic sine Arrhenius model provides adequate results. It does not consistently over-predict or under-predict flow stress with changing temperature or strain rate. The model generally has higher accuracy at higher strains. The model has fairly good accuracy, though it seems to be less accurate in predicting peak stress. The AARE for the Arrhenius model was 3.51%, and its RMSE was 2.88 MPa. This is by no means poor model performance, but there are some obvious inaccuracies in the model.

Because of the way strain is implemented, the Arrhenius model cannot predict flow stress past the lowest experimentally-obtained strain (in this case, a strain of about 0.92). Another outcome of the model's implementation of strain is that the Arrhenius model predicts the same general shape for each stress-strain curve. This is evident from a few kinks at 10%, 25%, 70% and 80% strain that are present in each flow curve. These kinks arise from the use of high order polynomials as fitting functions for the model constants, and they tend to cause inaccurate prediction of flow stress at low and high strain ($\epsilon < 0.1$ and $\epsilon > 0.8$). The final model constants used to obtain these results are presented below in Table 2. When expressed as a function of strain, each constant from Eq. (1) takes the general form

$$f(\varepsilon) = C_0 + C_1\varepsilon + C_2\varepsilon^2 + C_3\varepsilon^3 + C_4\varepsilon^4 + C_5\varepsilon^5 + C_6\varepsilon^6 + C_7\varepsilon^7 + C_8\varepsilon^8 \quad (18)$$

Table 2. Polynomial coefficients for hyperbolic sine Arrhenius model constants.

$f(\varepsilon)$	C_0	C_1	C_2	C_3	C_4	C_5	C_6	C_7	C_8
a	0.11717	-2.0862	21.523	-110.22	319.68	-552.17	563.01	-312.78	72.981
n	4.8508	23.208	-548.05	3554.8	-11598	21584	-23214	13438	-3241
Q	229.75	-1254.3	11794	-57511	$1.6038 \cdot 10^5$	-	$2.6431 \cdot 10^5$	-	32452
$\ln(A)$	26.172	-13.389	26.337	-37.137	39.811	-18.493	0	0	0

The constants C_6 , C_7 , and C_8 for $\ln(A)$ were chosen to be zero because a fifth-order polynomial fit the experimental data sufficiently well. It is usually desirable to use low-order polynomial functions in order to reduce the number of model constants, and other studies generally limit their use to fifth or sixth order polynomials [43,73,74]; these same studies often incorporate a lower sampling of experimental strains. Even with the eighth order polynomials used here, it seems that sharp features in a , n , and Q with respect to strain are captured poorly. This causes the kinks in the flow curve as well as the poor prediction at very low or very high strains. A weighting function could be used to increase accuracy of the polynomial fits at low strain; but the main issue lies with the technique of implementing polynomials, not the specific accuracy of the polynomials. As stated earlier, the original model developed by Sellars and Tegart does not have any terms relating to strain and is properly used under steady state or constant microstructure conditions [75]. It is unlikely that cast ZE20 will satisfy this condition even if deformed to high strains, given the differences in microstructure evolution that it exhibits.

Despite its flaws, the hyperbolic sine Arrhenius model is quite valuable as a standard against which to measure other models' performance. The extended Ludwik model achieved better agreement with the experimental data. Over the same strains where the Arrhenius model was valid, the Ludwik model had a slightly superior AARE and RMSE of 3.24% and 2.59 MPa even prior to model optimization. After optimization, the Ludwik model had an AARE of 2.74% and a RMSE of 2.23 MPa. Much like the Arrhenius model, the Ludwik model's worst point of predictive accuracy is near the peak stress. Unlike the Arrhenius model, the Ludwik model better predicts both low strain and high strain flow stress for most testing conditions. Because of its derivation from a hardening law, it is unsurprising that the modified Ludwik equation better predicts the hardening behavior of ZE20. The expansion of the Hollomon term into a hardening function gives the extended Ludwik equation high fidelity to ZE20's hardening behavior across different regimes of material behavior. Because the hardening function is a strain derivative and not a strain rate derivative, it is applicable to all experimental strains, unlike the Arrhenius model.

The optimized model constants used to obtain these results are detailed below. The strain rate sensitivity, m , and strength coefficient, K , in Eq. (4) are both described by linear functions of temperature:

$$m = 8.019 \cdot 10^{-4}T - 0.3626 \quad (19)$$

$$K = -0.4113 T + 346 \quad (20)$$

where K has units of MPa. Polynomial surfaces for the constants A , B , C , and D in Eq. (10) take the form

$$f(\dot{\varepsilon}, T) = C_1 + C_2 \ln \dot{\varepsilon} + C_3 T + C_4 (\ln \dot{\varepsilon})^2 + C_5 T \ln \dot{\varepsilon} + C_6 T^2 \quad (21)$$

The numeric coefficients for these surfaces are listed in Table 3.

Table 3. Coefficients for the polynomial surfaces fit to model constants A , B , C , and D

$f(\dot{\varepsilon}, T)$	C_1	C_2	C_3	C_4	C_5	C_6
A	47.076	0.26525	-0.0749	-0.010874	$9.9394 \cdot 10^{-4}$	$2.6387 \cdot 10^{-5}$
B	-39.057	-4.7308	0.066344	-0.084535	0.0069578	$-3.1699 \cdot 10^{-5}$
C	0.028347	0.27796	$7.1507 \cdot 10^{-4}$	0.0086193	$-3.4865 \cdot 10^{-4}$	$-1.5566 \cdot 10^{-6}$
D	-0.88045	-0.24373	0.002056	-0.012876	$2.6505 \cdot 10^{-4}$	$-6.3565 \cdot 10^{-7}$

In its present formulation, the extended Ludwik model has high accuracy over a moderate range of strain rates and temperatures. A large portion of the error in the extended Ludwik equation is due to polynomial fitting to the exponential function's constants. Over a small range, the constants of an exponential can have significant relative

differences while the function still evaluates approximately the same. Specifically speaking, the values of A , B , and C could vary significantly while not changing $d\ln(\sigma)/d\epsilon$ by much in Eq. (9). However, using exact numeric values instead of polynomial fits for A , B , C , and D , the model predicts with less than 1% error. This implies that, while the hardening function n' can predict material behavior with great accuracy, due to its power law formulation, its constants can be sensitive to small variations in stress and experimental errors. Overall, the validity of the general method is supported, but alternate forms for the hardening function and alternate optimization strategies may have more stable results.

In terms of model constants, the current formulation of the extended Ludwik model is approximately on par with the Arrhenius model. The extended Ludwik model uses 28 constants (24 in Table 3 and four from Eq. (19) and (20)) while the formulation used here for the Arrhenius model has 27 constants, all from Table 2. There is little room for improvement for the Arrhenius model, as a , n , Q , and A often take complex forms, necessitating the use of high-order polynomials. Conversely, the extended Ludwik model likely has much room for improvement because so many constants are grouped into n' . In other words, n' is likely over-defined in the model's present formulation. This effectively permits model optimization; because A , B , C , and D have no physical significance, their values may be changed (within reason and with verification that n' still fits Eq. (8)) in order to minimize model error. Similar optimization is not possible for the Sellars-Tegart model, where non-physical results are often obtained. Sacrificing some of the extended Ludwik model's potential for optimization, the form of A , B , C , and/or D could be limited to either strain rate or temperature dependence in order to reduce the number of model constants. Alternately, simpler linear polynomial surfaces could be chosen for A , B , C , and/or D . Having higher accuracy with a similar number of constants while also having options for optimization or reduction in the number of model constants shows the potential of the extended Ludwik model.

Several possible changes in form could also increase the performance of the extended Ludwik model. One of the advantages of the Hyperbolic Sine Arrhenius equation is that it is applicable over a wide range of strain rates and temperatures. It can predict flow stress well in regimes where strain rate sensitivity is dependent on strain rate (regimes where the power law is not valid) [75]. The extended Ludwik equation could easily incorporate rate-dependence of strain rate sensitivity, using a method for m similar to that for n' , in order to further increase its range of applicability. While not presented here, several other forms for $d\ln(\sigma)/d\epsilon$ in Eq. (8) were considered, including power law, rational, and polynomial forms. Alternate solution methods were also tried, by substituting exponential, power, rational, and polynomial functions directly for n' in order to eliminate the extra constant necessitated by solution of the differential equation in (9). Many attempts were successful, but the present formulation had the highest predictive accuracy while also having constants in an easily reportable form. The emphasis here is on the general solution method. In other materials, some of these alternate methods may better fit the material behavior or may improve the utility of the model by reducing the number of necessary model constants.

4.3 Processing Maps and Characterization

The processing maps obtained from the experimental data are shown below in Fig. 3. Two domains and two instability regions in Fig. 3 were identified using conventional guidelines. Domain I exists between $10^{-1.5} \text{ s}^{-1}$ and $10^{-2.5} \text{ s}^{-1}$ above 400°C and 5% strain. Domain II exists between 300°C and 400°C below $10^{-2.5} \text{ s}^{-1}$, shifting to lower temperatures at higher strains, and finally disappearing at 55% strain. Instability Region I sweeps across most of the temperatures and strain rates, leaving two islands of stability: one at low strain rate and high temperature, and one at high strain rate and low temperature. The stable region at low temperature and high rate gradually moves to even lower temperatures and higher strain rates as Instability Region I moves to lower temperatures and strain rates with increasing strain. Instability Region II lies between 400°C and 450°C at 10^{-3} s^{-1} between 20% and 45% strain.

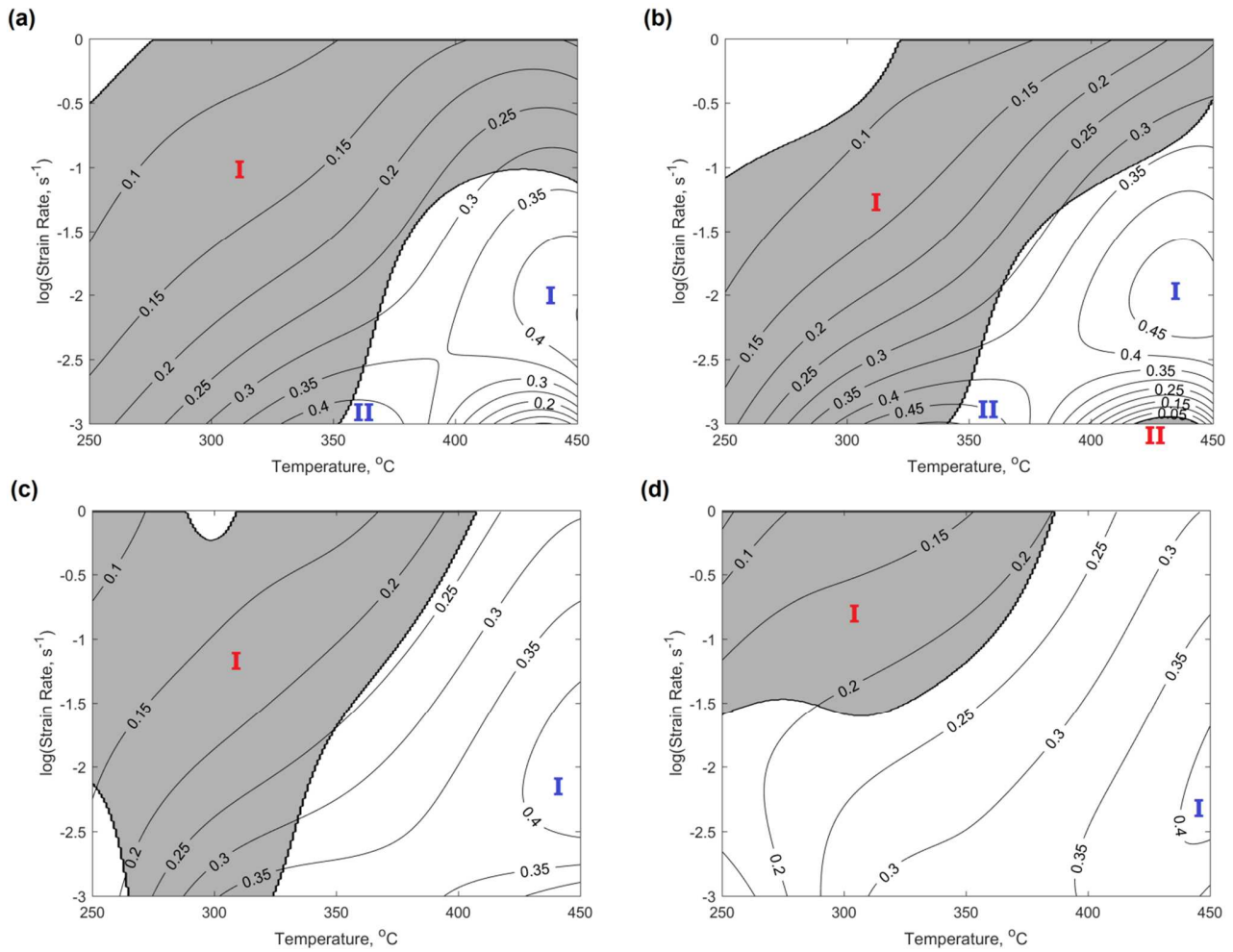


Fig. 3. Processing maps for ZE20 at (a) 15% strain, (b) 35% strain, (c) 65% strain, and (d) 90% strain. Domains and Instability Regions are numbered in blue and red, respectively. Shading indicates regions where the stability criterion (Eq. (17)) is not met.

As noted previously, processing maps built using Equations (15) and (17) only implicitly contain information about the microstructural processes taking place. Furthermore, all metallurgical processes which could dissipate power are included in the single efficiency parameter. With this construction, explicit rules about processing and microstructures do not exist. Instead, the generally accepted rule is to choose processing temperatures and strain rates where DRX will occur, usually found at a maximum of efficiency between 30% and 55%, depending on the material's stacking fault energy [76]. With this convention, Domain I and Domain II are good choices for primary processing.

These expectations are mostly consistent with the conventional flow curve analysis. Referring back to the discussion about Fig. 1, low Z testing conditions produce nearly flat flow curves, and DRX was predicted throughout this region. Domain I and Domain II lie in this region, and the high η values at high temperature and low strain rate in Fig. 3 (c) and (d) reflect this. Contrary to the classical analysis, Instability Region II exists between 400°C and 450°C at 10^{-3} s^{-1} , which should have little or no DRX. Because this lies between the initial testing temperatures, it could not be seen from the flow curves. Moderate and high Z regions are also fairly consistent with conventional analysis. The softening visible at moderate and high strains in these flow curves correlates well with Instability Region I. Because processing maps are calculated on the basis of strain rate sensitivity, they do not exactly reflect the classical assumption that work softening causes plastic flow instability. Take for example the flow curves for 400°C and 450°C at 1.0 s^{-1} – softening is clearly evident at high strain in Fig. 1 (d), but stability is predicted in Fig. 3 (d).

The microstructural processes occurring in these domains and instability regions were verified with EBSD. For reference, the initial microstructure and texture of an exemplar specimen are shown in Fig. 4 along with specimen reference directions. The orientation color map (or IPF map) shows that the as-cast material has a globular dendritic microstructure with relatively equiaxed grains. The average grain size was measured as $380 \mu\text{m}$. Clusters of non-indexed

scan points visible in the IPF map correspond to second phase particles in the grain interiors and at grain boundaries. The pole figures show a few peaks in texture intensity, but they do not correspond to any typical texture component for Mg. Instead, since relatively few grains were sampled in the scan area, the pole figures show that a variety of orientations are sampled for such few grains. The as-cast material therefore has a fairly random texture.

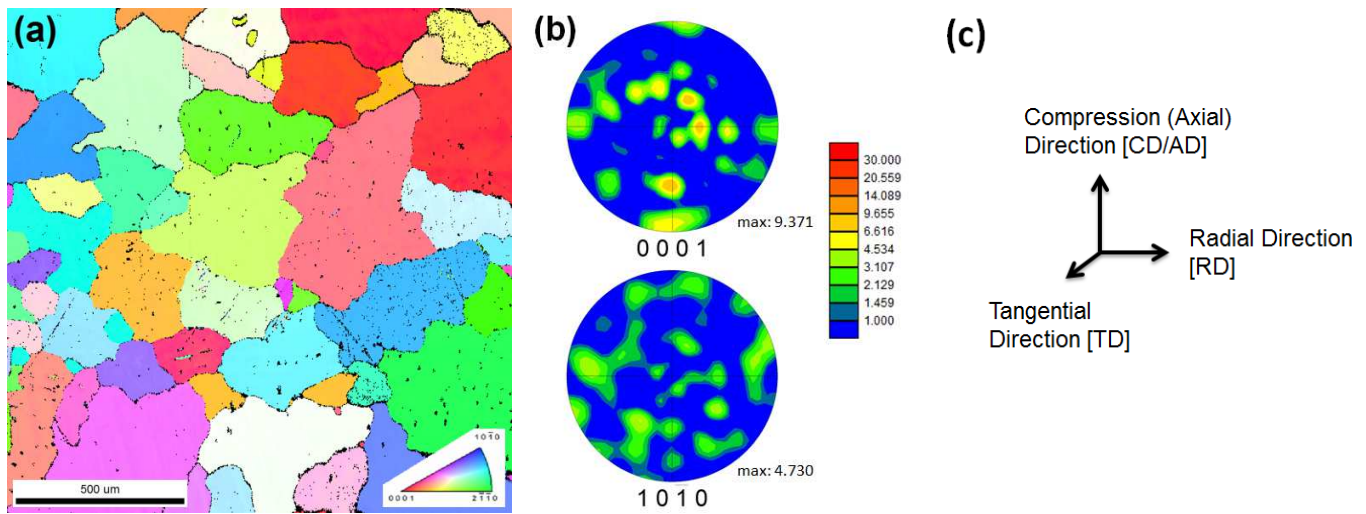


Fig. 4. Microstructure and texture of as-cast ZE20: (a) IPF map with key, (b) basal and prismatic pole figures of scan area, and (c) specimen directions. Colors for (a) are plotted in [AD]. IPF key in (a), scale in (b), and specimen directions in (c) are consistent for all other figures.

Consistent with the both the conventional and processing map predictions, Domain I exhibited significant DRX. Fig. 5 shows the microstructure and texture of a specimen tested in Domain I at 450°C and 10^{-2} s^{-1} to 100% strain, partitioned into deformed and recrystallized grains. Recrystallization is obviously discontinuous, with bands of recrystallized grains separating large deformed grains. Fig. 5 (c) shows that the texture of the deformed material is nearly basal, with the predominant texture component in the compression direction about 20° from [0001]. The recrystallized region has the same texture component with a lower intensity.

The bulk non-basal texture is noteworthy. Similar textures occur in the form of split RD peaks in sheet alloys of the same Mg-Zn-RE alloy class [77]. Such textures have been attributed to increased activity of pyramidal $\langle c+a \rangle$ slip activity [78,79]. In this case, the activation of pyramidal $\langle c+a \rangle$ slip and associated DRX across a range of strain rates and temperatures should allow efficient processing to very high strains. Aside from the texture, the microstructure in Domain I is not remarkable. A more homogeneous and finer-grained material is usually desired. The specimen from Fig. 5 was processed at peak efficiency; processing at the lower temperature boundary of Domain I would result in a smaller recrystallized grain size and would also be more industrially viable.

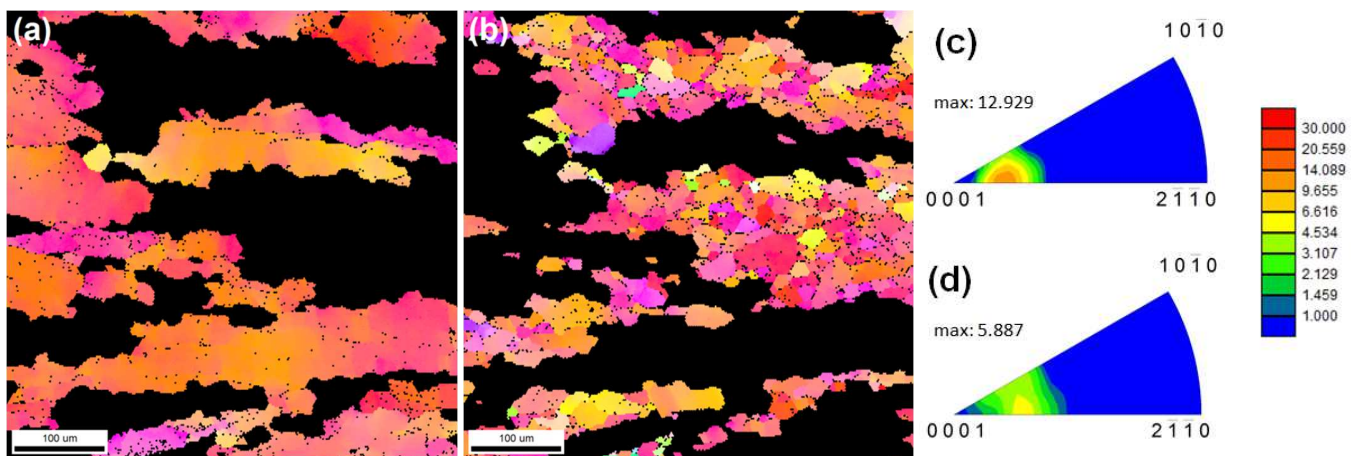


Fig. 5. Microstructure and texture of specimen tested at 450°C and 10^{-2} s^{-1} (Domain I) to 100% strain: (a) Orientation color map of deformed grains, (b) Orientation color map of recrystallized grains, (c) IPF of the deformed grains for the compression direction, and (d) IPF of the recrystallized grains in the compression direction.

Fig. 6 shows the microstructure of a specimen tested in Domain II at 350°C and 10^{-3} s^{-1} to 35% strain. Domain II lies at the edge of Instability Region I, and the specimen shown in Fig. 6 passed partially through Instability Region I. As such, some flow localization is present. A band of localized flow is visible from upper left to lower right across both IPF maps. Much of the recrystallization visible in Fig. 6 (b) is associated with this deformation band. Only a few recrystallized grains are visible at grain boundaries outside the deformation band. The parent material does not exhibit a basal texture. The imposed strain of compression testing may be relieved by flow localization as these grains reorient to “hard” orientations; combined with the relatively low strain of the test, this may mean that the microstructure has not yet reached a stable (basal) orientation. The texture of the recrystallized grains is much more random, reflecting the more random orientation of the parent material which was present when these grains nucleated at this relatively low strain. Despite a non-basal texture, the flow localization present here suggests the need for very fine process control to avoid Instability Region I if Domain II were to be used for processing. Furthermore, Domain II vanishes at moderate strain, far below the strains imposed during rolling or extrusion. Overall, the utility of Domain II for processing is questionable.

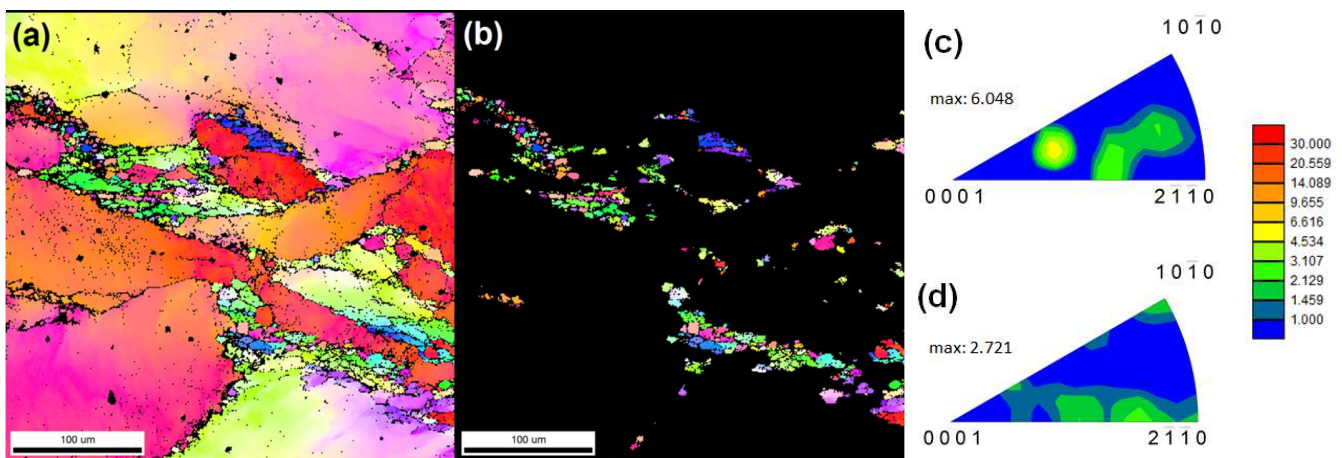


Fig. 6. Microstructure and texture of specimen tested at 350°C and 10^{-3} s^{-1} (Domain II) to 35% strain: (a) Orientation color map, (b) Orientation color map of recrystallized grains, (c) IPF showing the bulk texture in the compression direction, and (d) IPF of the recrystallized grains in the compression direction.

Three types of plastic instability were evident in Instability Region I. The most prevalent, flow localization, was evident in all specimens from Instability Region I. Generally, localized flow occurred in wavy, intersecting bands perpendicular to the compression axis throughout an entire specimen. The intensity of flow localization increased with decreasing temperature and increased slightly with increasing strain rate. Regions of localized flow were only observed in a partially or fully recrystallized state, which fits the established recrystallization and flow softening mechanism for the phenomenon [80]. While localized flow is not particularly visible in orientation color maps, the recrystallization bands with which it is associated are easily identifiable via EBSD. Fig. 7 shows EBSD results from a specimen in Instability Region I where flow localization was evident. A fairly strong, nearly-basal texture is shown for the deformed grains, and a much weaker texture of the same character is evident for the recrystallized grains. Retained basal texture with weakened intensity is very common in Mg alloys.

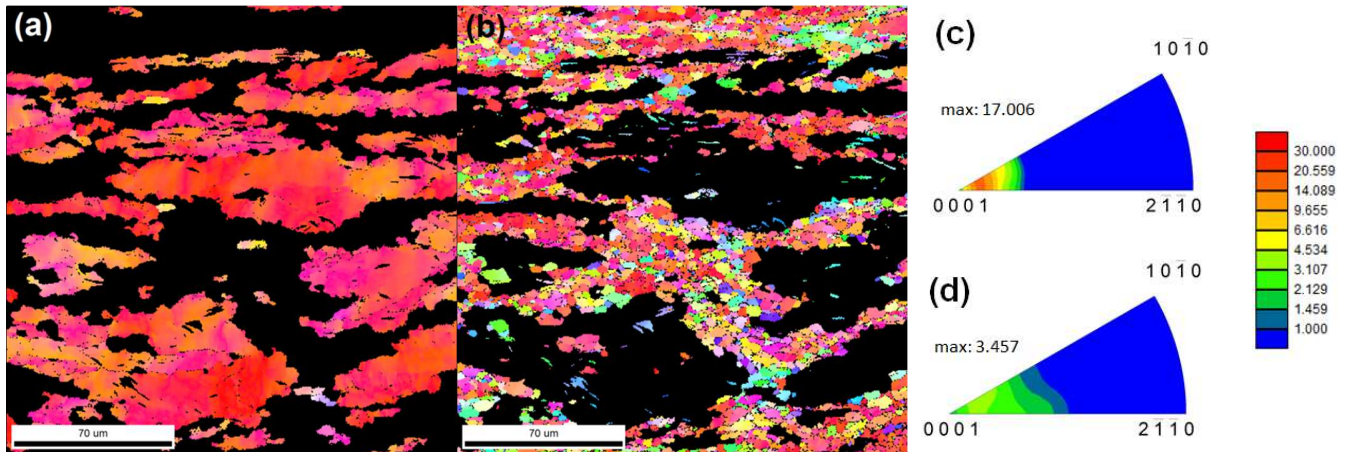


Fig. 7. Microstructure and texture of specimen tested at 350°C and 10^{-2} s^{-1} (Instability Region I) to 100% strain: (a) Orientation color map of deformed grains, (b) Orientation color map of recrystallized grains in regions of localized flow, (c) IPF of the deformed grains in the compression direction, and (d) IPF of the recrystallized grains in the compression direction.

Adiabatic shear bands were also visible in some specimens from Instability Region I. Shear bands were only evident at higher strain rates and lower temperatures in Instability Region I. When observed, shear bands were aligned roughly 45° to the compression axis and were fully recrystallized. Fig. 8 shows the microstructure and texture of shear bands and their parent material. The texture intensity of the parent material is not very meaningful, as only a single grain was sampled, but the parent material's basal texture component is relevant. Fig. 8 (b) and (d) show clear evidence of SBN giving rise to a non-basal orientation. A weak (3035) texture component in the compression is observed for the recrystallized grains.

On the surface, it would seem that the microstructures of specimens tested in Instability Region I would be undesirable for any wrought product, often containing heavily localized flow, bulk basal texture, and low volume fractions of recrystallization. However, certain aspects of the microstructure and texture of specimens from Instability Region I do have merit. The unrecrystallized grains in the specimen from Fig. 7 had a basal texture component with a greater intensity than that of the specimen from Domain I (Fig. 5). This is fairly undesirable, but both specimens has a similar area fraction of recrystallized material; and the texture intensity of recrystallized grains in the specimen from Instability Region I was actually lower than that of the recrystallized grains in Domain I. The recrystallization texture from the shear bands (both in texture component and intensity) is also superior to that of the specimen from Domain I. If a material were processed under these conditions, subsequent annealing would cause grain growth in these recrystallized regions at the expense of highly deformed grains. The result would be an overall weakening of global texture (or local strengthening of non-basal texture) as well as refinement of the microstructure. This presents the potential for a high performance sheet or extrusion but would necessarily introduce added cost with an additional processing step.

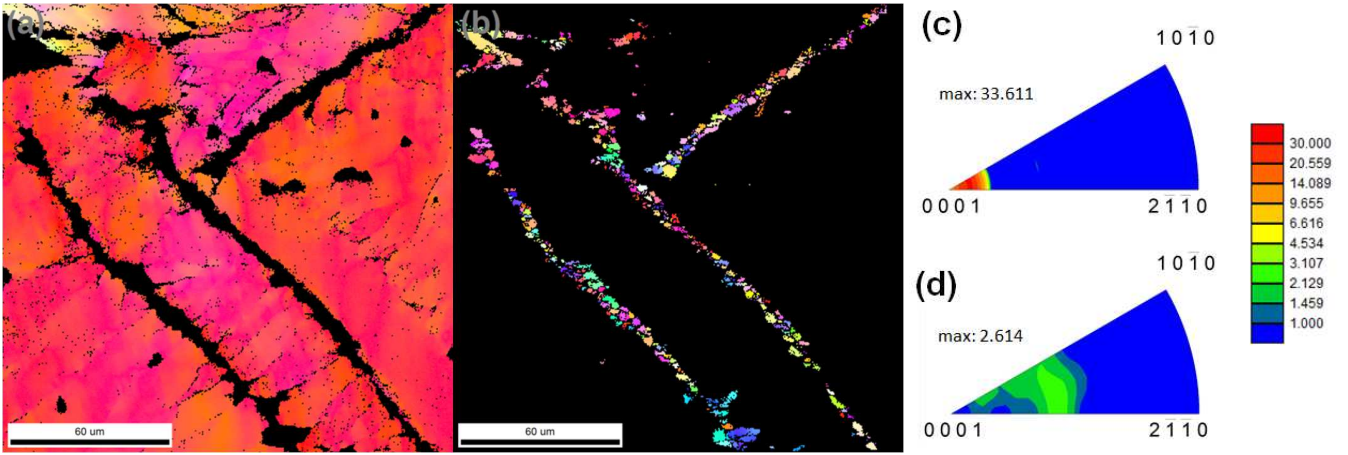


Fig. 8. Microstructure and texture of specimen tested at 300°C and 10^{-1} s^{-1} (Instability Region I) to 100% strain: (a) Orientation color map of deformed matrix, (b) Orientation color map of shear bands, (c) IPF of the matrix in the compression direction, and (d) IPF of the shear bands in the compression direction.

Though not shown here, shear cracking was also observed in some specimens from Instability Region I. Macroscopic shear cracking was observed in some specimens tested at 250°C, 300°C, and 450°C and 1.0 s^{-1} as well as 250°C and 10^{-1} s^{-1} . Sparse microcracking was also observed in specimens tested at 250°C and 10^{-2} s^{-1} and 10^{-3} s^{-1} as well as 300°C and 10^{-3} s^{-1} . Cracking of any extent creates a flaw which can lead to failure in service. No matter the type of cracking observed, these conditions are unacceptable for processing and mark the limits of warm formability for ZE20.

Instability Region II did not exhibit flow localization in the same manner as Instability Region I. For Instability region II, the stability criterion in Eq. (17) is not satisfied because η is negative. From Eq. (15), this implies that ZE20 has negative strain rate sensitivity in Instability Region II. Such regions are expected to undergo DSA, which is mechanistically associated with microscopic strain localization [76]. Jiang, Jonas, and Mishra reported occurrence of the rare earth texture component while processing under conditions of DSA [36]. Though they did not show microstructures, they argued that extremely localized flow associated with DSA could serve as a nucleation site for shear banding, noting that shear bands have been shown to recrystallize into rare earth texture orientations [33,81]. Unfortunately, no shear bands were evident in the specimens tested in Instability Region II, and the rare earth texture component was not evident. The absence of shear banding could be due to the low strain at which DSA is expected to occur, as there may not have been enough strain localization to nucleate shear banding. It is also possible that the strain rate and temperature used seem to lie only at the very periphery of Instability Region II, and DSA was only weakly present (again, not enough to nucleate shear bands).

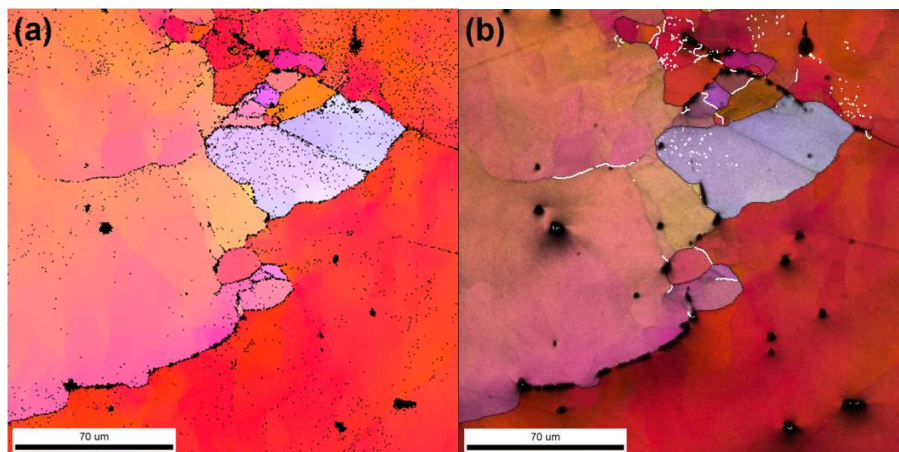


Fig. 9. Microstructures of a specimen compressed to 35% strain at 430°C and 10^{-3} s^{-1} (Instability Region II): (a) Orientation color map, and (b) Orientation color map with image quality superimposed and subgrain boundaries ($5\text{-}15^\circ$ misorientation) with low confidence index points included for clarity.

Instead of shear bands, the microstructures of specimens deformed to 35% strain in Instability Region II were nearly homogeneous, having no obvious flow localization. Specimens also had little recrystallization relative to other specimens

deformed to the same strain, especially when compared to Domain II specimens (Fig. 6). Further inspection showed severe grain boundary bulging, as is evident in Fig. 9. It is most likely that bulging is the mechanism by which DRX initiates in this temperature and strain rate regime. Excessive bulging and pinning could also be evidence of DSA, as these indicate strong solute interaction with grain boundaries. This type of evidence for DSA is weak, however, as other specimens had similar features. Classical microstructural evidence of DSA, such as sheared precipitates and changes in dislocation substructure, would be more visible using transmission electron microscopy (TEM). Regardless of the activity of DSA in Instability Region II, shear banding, the microstructural feature with potential for texture modification, was not present. This, coupled with the low volume fraction of recrystallization and the low strain at which Instability Region II occurs makes this region unsuitable for primary production of wrought materials.

The above observations and analysis can be combined into a single set of recommendations for primary processing. These are visually presented in Fig. 10 by superimposing the processing maps from Fig. 3 and adding observed microstructural failure conditions.

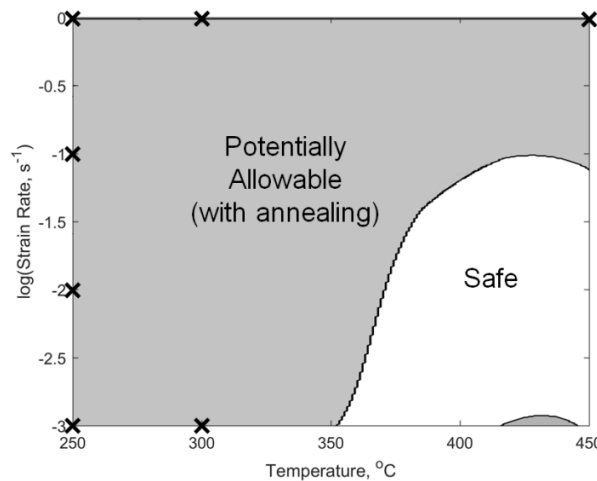


Fig. 10. Summary of processing conditions for ZE20. Shaded areas indicate the presence of an instability region. X indicates conditions under which cracking was observed.

The most industrially preferable processing conditions lie at high strain rates and low temperatures, translating to higher production speed and lower energy cost from heating. For the safe region, this points to higher strain rates than Domain II or Instability Region II, neither of which showed particularly interesting microstructural or texture traits. Desired processing within the safe region would also occur at lower temperatures than those for Domain I. The beneficial texture observed in Domain I is present in specimens tested at 400°C and 10^{-2} s^{-1} , but the recrystallized grains are finer while still representing a similar volume fraction of the material, resulting in a superior microstructure. This analysis is supported by Luo et al. who studied extrudability of ZE20 relative to AZ31 [1]. Luo et al. found superior extrudability for ZE20 at 425°C and several extrusion speeds, which translate to estimated mean strain rates of $10^{-0.80} \text{ s}^{-1}$ to $10^{-0.09} \text{ s}^{-1}$.

Outside of the “safe” region, processing at lower temperature and higher strain rate increases the frequency of shear banding. Higher concentration of shear bands would actually be desirable if one were to anneal the material in order to grow the shear-band-nucleated grains and take advantage of the resulting non-basal texture. For this reason, the region is marked as “potentially allowable.” Processing at too low temperature or too high strain rate risks shear cracking, though. The exact boundary where shear cracking begins was not investigated in detail. It is important to stress that the conditions marked as unsafe due to shear cracking in Fig. 10 are recommendations for primary processing and do not necessarily preclude subsequent forming operations in these areas. For example, if a sheet or tube had a favorable microstructure and texture from primary rolling or extrusion in Domain I, it may be possible to carry out subsequent sheet forming or tube bending at 250°C.

These recommendations lay the grounds for future study related to processing. Much study would be needed to determine whether annealing in the potentially allowed region would actually produce a beneficial microstructure or texture. Given the limited recrystallization observed within the shear bands in Instability Region I, this regime may lend itself to multiple-step interrupted warm forming processes, such as multi-pass rolling. For a sheet undergoing repeated rolling and annealing, hold time at temperature between process steps should facilitate grain growth of the non-basal grains, resulting in greater formability. For the safe region, we already show that a favorable recrystallization texture forms, but some work is required to see if annealing or further strain can achieve a higher volume fraction of

recrystallization. Besides microstructure, future work is also needed to assess the mechanical properties and formability of components produced by primary processing in the recommended regions.

Conclusions

The hot deformation behavior of wrought Mg alloy ZE20 was investigated between 250°C and 450°C from 10^{-3} s^{-1} to 1.0 s^{-1} . Several deformation and recrystallization phenomena were identified. While sophisticated models, such as crystal plasticity finite element methods, could be used to correlate the operation of these phenomena with the mechanical behavior for academic purposes, simpler constitutive descriptions of material behavior are provided here for industrial applications. The hyperbolic sine Arrhenius equation and the extended Ludwik equation are both considered. Modifications to the extended Ludwik equation and a general strain hardening function are presented. The modified Ludwik equation was found to have higher predictive accuracy than the hyperbolic sine Arrhenius equation and was found to respond more favorably to optimization. Potential for future modelling work and alternate approaches for application to other material systems are outlined.

Processing maps constructed using the experimental data are presented. Domains are identified, and guided microstructural characterization allows identification of acceptable processing conditions. A safe region for processing occurs between 375°C and 450°C, from 10^{-1} s^{-1} to $10^{-2.5} \text{ s}^{-1}$. Non-basal texture similar to split RD sheet texture was observed in this region, and it may be applicable to extrusion. Another region of potentially allowable processing extends as low as 300°C at strain rates up to 10^{-1} s^{-1} . Subsequent annealing would take advantage of non-basal shear band nucleation to make this region potentially suitable for rolling or forging.

Acknowledgements

This work is partially supported by the United States Automotive Materials Partnership (USAMP). The authors acknowledge technical discussions with Drs. Raj K. Mishra and Anil K. Sachdev of General Motors and Dr. Joy Forsmark of Ford Motor Company. The authors also acknowledge helpful discussions with Prof. Robert Wagoner of the Ohio State University.

This material is based in part upon work supported by the Department of Energy National Energy Technology Laboratory under Award Number DE-EE0003583. This report was prepared as an account of work sponsored by an agency of the United States Government. Neither the United States Government nor any agency thereof, nor any of their employees, makes any warranty, express or implied, or assumes any legal liability or responsibility for the accuracy, completeness, or usefulness of any information, apparatus, product, or process disclosed, or represents that its use would not infringe privately owned rights. Reference herein to any specific commercial product, process, or service by trade name, trademark, manufacturer, or otherwise does not necessarily constitute or imply its endorsement, recommendation, or favoring by the United States Government or any agency thereof. The views and opinions of authors expressed herein do not necessarily state or reflect those of the United States Government or any agency thereof.

References

- [1] A.A. Luo, R.K. Mishra, A.K. Sachdev, High-ductility magnesium-zinc-cerium extrusion alloys, *Scr. Mater.* 64 (2011) 410–413.
- [2] M.O. Pekguleryuz, K.U. Kainer, A. Arslan Kaya, F. Witte, *Fundamentals of Magnesium Alloy Metallurgy*, 2013. doi:10.1533/9780857097293.342.
- [3] A.A. Luo, *Wrought Magnesium Alloys and Manufacturing Processes for Automotive Applications*, SAE Tech. Pap. 01 (2005). doi:10.4271/2005-01-0734.
- [4] A. Staroselsky, L. Anand, A constitutive model for hcp materials deforming by slip and twinning: Application to magnesium alloy AZ31B, *Int. J. Plast.* 19 (2003) 1843–1864. doi:10.1016/S0749-6419(03)00039-1.
- [5] S.R. Agnew, Ö. Duygulu, Plastic anisotropy and the role of non-basal slip in magnesium alloy AZ31B, in: *Int. J. Plast.*, 2005: pp. 1161–1193. doi:10.1016/j.ijplas.2004.05.018.
- [6] M.R. Barnett, Twinning and the ductility of magnesium alloys. Part I: “Tension” twins, *Mater. Sci. Eng. A*. 464 (2007) 1–7. doi:10.1016/j.msea.2006.12.037.
- [7] M.R. Barnett, Twinning and the ductility of magnesium alloys. Part II. “Contraction” twins, *Mater. Sci. Eng. A*. 464 (2007) 8–16. doi:10.1016/j.msea.2007.02.109.
- [8] A. Jain, S.R. Agnew, Modeling the temperature dependent effect of twinning on the behavior of magnesium alloy

- AZ31B sheet, *Mater. Sci. Eng. A.* 462 (2007) 29–36. doi:10.1016/j.msea.2006.03.160.
- [9] S.R. Agnew, D.W. Brown, C.N. Tomé, Validating a polycrystal model for the elastoplastic response of magnesium alloy AZ31 using in situ neutron diffraction, *Acta Mater.* 54 (2006) 4841–4852. doi:10.1016/j.actamat.2006.06.020.
- [10] A. Kula, X. Jia, R.K. Mishra, M. Niewczas, Flow stress and work hardening of Mg-Y alloys, *Int. J. Plast.* 92 (2017) 96–121. doi:10.1016/j.ijplas.2017.01.012.
- [11] N. Stanford, M.R. Barnett, Solute strengthening of prismatic slip, basal slip and twinning in Mg and Mg-Zn binary alloys, *Int. J. Plast.* 47 (2013) 165–181. doi:10.1016/j.ijplas.2013.01.012.
- [12] Y. Wang, J.C. Huang, Texture analysis in hexagonal materials, *Mater. Chem. Phys.* 81 (2003) 11–26. doi:10.1016/s0254-0584(03)00168-8.
- [13] K.K. Alaneme, E.A. Okotete, Enhancing plastic deformability of Mg and its alloys—A review of traditional and nascent developments, *J. Magnes. Alloy.* 5 (2017) 460–475. doi:10.1016/j.jma.2017.11.001.
- [14] E.A. Ball, P.B. Prangnell, Tensile-compressive yield asymmetries in high strength wrought magnesium alloys, *Scr. Metall. Mater.* 31 (1994) 111–116. doi:10.1016/0956-716X(94)90159-7.
- [15] S.R. Agnew, Deformation mechanisms of magnesium alloys, in: *Adv. Wrought Magnes. Alloy. Fundam. Process. Prop. Appl.*, Elsevier, 2012: pp. 63–104. doi:10.1016/B978-1-84569-968-0.50002-8.
- [16] M.R. Barnett, Z. Keshavarz, A.G. Beer, D. Atwell, Influence of grain size on the compressive deformation of wrought Mg-3Al-1Zn, *Acta Mater.* 52 (2004) 5093–5103. doi:10.1016/j.actamat.2004.07.015.
- [17] M.A. Meyers, O. Vöhringer, V.A. Lubarda, The onset of twinning in metals: A constitutive description, *Acta Mater.* 49 (2001) 4025–4039. doi:10.1016/S1359-6454(01)00300-7.
- [18] Y. Chino, K. Kimura, M. Mabuchi, Twinning behavior and deformation mechanisms of extruded AZ31 Mg alloy, *Mater. Sci. Eng. A.* 486 (2008) 481–488. doi:10.1016/j.msea.2007.09.058.
- [19] K. Yan, J. Bai, H. Liu, Z.Y. Jin, The precipitation behavior of MgZn₂ and Mg₄Zn₇ phase in Mg-6Zn (wt.%) alloy during equal-channel angular pressing, *J. Magnes. Alloy.* 5 (2017) 336–339. doi:10.1016/j.jma.2017.08.007.
- [20] I.J. Beyerlein, L.S. Tóth, Texture evolution in equal-channel angular extrusion, *Prog. Mater. Sci.* 54 (2009) 427–510. doi:10.1016/j.pmatsci.2009.01.001.
- [21] A.S. Khan, A. Pandey, T. Gnäupel-Herold, R.K. Mishra, Mechanical response and texture evolution of AZ31 alloy at large strains for different strain rates and temperatures, *Int. J. Plast.* 27 (2011) 688–706. doi:10.1016/j.ijplas.2010.08.009.
- [22] H. Wang, P.D. Wu, M.A. Gharghouri, Effects of basal texture on mechanical behaviour of magnesium alloy AZ31B sheet, *Mater. Sci. Eng. A.* 527 (2010) 3588–3594. doi:10.1016/j.msea.2010.02.050.
- [23] T. Al-Samman, X. Li, S.G. Chowdhury, Orientation dependent slip and twinning during compression and tension of strongly textured magnesium AZ31 alloy, *Mater. Sci. Eng. A.* 527 (2010) 3450–3463. doi:10.1016/j.msea.2010.02.008.
- [24] F. Abbassi, M. Srinivasan, C. Loganathan, R. Narayanasamy, M. Gupta, Experimental and numerical analyses of magnesium alloy hot workability, *J. Magnes. Alloy.* 4 (2016) 295–301. doi:10.1016/j.jma.2016.10.004.
- [25] Q. Liu, X. Zhou, H. Zhou, X. Fan, K. Liu, The effect of extrusion conditions on the properties and textures of AZ31B alloy, *J. Magnes. Alloy.* 5 (2017) 202–209. doi:10.1016/j.jma.2017.03.002.
- [26] A. Tripathi, S.V.S.N. Murty, P.R. Narayanan, Microstructure and texture evolution in AZ31 magnesium alloy during caliber rolling at different temperatures, *J. Magnes. Alloy.* 5 (2017) 340–347. doi:10.1016/j.jma.2017.07.001.
- [27] L.L.C. Catorceno, H.F.G. de Abreu, A.F. Padilha, Effects of cold and warm cross-rolling on microstructure and texture evolution of AZ31B magnesium alloy sheet, *J. Magnes. Alloy.* 6 (2018) 121–133. doi:10.1016/j.jma.2018.04.004.
- [28] L. Guo, F. Fujita, Influence of rolling parameters on dynamically recrystallized microstructures in AZ31 magnesium alloy sheets, *J. Magnes. Alloy.* 3 (2015) 95–105. doi:10.1016/j.jma.2015.04.004.
- [29] S. You, Y. Huang, K.U. Kainer, N. Hort, Recent research and developments on wrought magnesium alloys, *J. Magnes. Alloy.* 5 (2017) 239–253. doi:10.1016/j.jma.2017.09.001.
- [30] P. Liu, H. Jiang, Z. Cai, Q. Kang, Y. Zhang, The effect of Y, Ce and Gd on texture, recrystallization and mechanical property of Mg-Zn alloys, *J. Magnes. Alloy.* 4 (2016) 188–196. doi:10.1016/j.jma.2016.07.001.
- [31] L.W.F. Mackenzie, M.O. Pekguleryuz, The recrystallization and texture of magnesium-zinc-cerium alloys, *Scr. Mater.* 59 (2008) 665–668. doi:10.1016/j.scriptamat.2008.05.021.
- [32] J.D. Robson, D.T. Henry, B. Davis, Particle effects on recrystallization in magnesium-manganese alloys: Particle-stimulated nucleation, *Acta Mater.* 57 (2009) 2739–2747. doi:10.1016/j.actamat.2009.02.032.
- [33] N. Stanford, M.R. Barnett, The origin of “rare earth” texture development in extruded Mg-based alloys and its effect on tensile ductility, *Mater. Sci. Eng. A.* 496 (2008) 399–408. doi:10.1016/j.msea.2008.05.045.
- [34] R.K. Mishra, A.K. Gupta, P.R. Rao, A.K. Sachdev, A.M. Kumar, A.A. Luo, Influence of cerium on the texture and ductility of magnesium extrusions, *Scr. Mater.* 59 (2008) 562–565. doi:10.1016/j.scriptamat.2008.05.019.

- [35] N. Stanford, Micro-alloying Mg with Y, Ce, Gd and La for texture modification—A comparative study, *Mater. Sci. Eng. A.* 527 (2010) 2669–2677. doi:10.1016/j.msea.2009.12.036.
- [36] L. Jiang, J.J. Jonas, R. Mishra, Effect of dynamic strain aging on the appearance of the rare earth texture component in magnesium alloys, *Mater. Sci. Eng. A.* 528 (2011) 6596–6605. doi:10.1016/j.msea.2011.05.027.
- [37] A.A. Luo, R.K. Mishra, A.K. Sachdev, High ductility/strength magnesium alloys, US8361251, 2013. <http://www.google.com/patents/US8361251>.
- [38] L. Gao, A.A. Luo, Hot deformation behavior of as-cast Mg-Zn-Mn-Ce alloy in compression, *Mater. Sci. Eng. A.* 560 (2013) 492–499. doi:10.1016/j.msea.2012.09.094.
- [39] S. Bingöl, W. Misiólek, Prediction of the true stress of ZE20 magnesium alloy at different temperatures and strain rates, *Stroj. Vestnik/Journal Mech. Eng.* 61 (2015) 610–617. doi:10.5545/sv-jme.2015.2785.
- [40] S. Sutton, A.A. Luo, Hot Compression Behavior of Magnesium Alloys ZE20 AND AM30, in: *Magnes. Technol.* 2015, John Wiley & Sons, Inc., Hoboken, NJ, USA, 2015: pp. 25–28. doi:10.1002/9781119093428.ch8.
- [41] C.M. Sellars, W.J. McTegart, On the mechanism of hot deformation, *Acta Metall.* 14 (1966) 1136–1138. doi:10.1016/0001-6160(66)90207-0.
- [42] J.J. Jonas, C.M. Sellars, W.J.M. Tegart, Strength and structure under hot-working conditions, *Int. Mater. Rev.* 14 (1969) 1–24. doi:10.1179/095066069790138056.
- [43] Y.C. Lin, Y.-C. Xia, X.-M. Chen, M.-S. Chen, Constitutive descriptions for hot compressed 2124-T851 aluminum alloy over a wide range of temperature and strain rate, *Comput. Mater. Sci.* 50 (2010) 227–233. doi:10.1016/j.commatsci.2010.08.003.
- [44] M.J. Roy, D.M. Maijer, L. Dancoine, Constitutive behavior of as-cast A356, *Mater. Sci. Eng. A.* 548 (2012) 195–205. doi:10.1016/j.msea.2012.03.106.
- [45] J. Liu, Z. Cui, C. Li, Modelling of flow stress characterizing dynamic recrystallization for magnesium alloy AZ31B, *Comput. Mater. Sci.* 41 (2008) 375–382. doi:10.1016/j.commatsci.2007.04.024.
- [46] S.F. Medina, C.A. Hernandez, General expression of the Zener-Hollomon parameter as a function of the chemical composition of low alloy and microalloyed steels, *Acta Mater.* 44 (1996) 137–148. doi:10.1016/1359-6454(95)00151-0.
- [47] F. cai Ren, J. Chen, Modeling Flow Stress of 70Cr3Mo Steel Used for Back-Up Roll During Hot Deformation Considering Strain Compensation, *J. Iron Steel Res. Int.* 20 (2013) 118–127. doi:10.1016/S1006-706X(13)60206-X.
- [48] A. Hadadzadeh, M.A. Wells, Analysis of the hot deformation of ZK60 magnesium alloy, *J. Magnes. Alloy.* (2017). doi:10.1016/j.jma.2017.09.002.
- [49] W.M. van Haaften, B. Magnin, W.H. Kool, L. Katgerman, Constitutive behavior of as-cast AA1050, AA3104, and AA5182, *Metall. Mater. Trans. A.* 33 (2002) 1971–1980. doi:10.1007/s11661-002-0030-8.
- [50] M.L. Nedreberg, Ph.D. Thesis, University of Oslo, 1991.
- [51] J.M. Drezet, A.B. Phillion, As-cast residual stresses in an aluminum alloy aa6063 billet: Neutron diffraction measurements and finite element modeling, *Metall. Mater. Trans. A Phys. Metall. Mater. Sci.* 41 (2010) 3396–3404. doi:10.1007/s11661-010-0424-y.
- [52] W.B. Morrison, The effect of grain size on the stress-strain relationship in low-carbon steel, *ASM Trans Quart.* 59 (1966) 824–846.
- [53] Y.V.R.K. Prasad, H.L. Gegel, S.M. Doraivelu, J.C. Malas, J.T. Morgan, K.A. Lark, D.R. Barker, Modeling of dynamic material behavior in hot deformation: Forging of Ti-6242, *Metall. Trans. A.* 15 (1984) 1883–1892. doi:10.1007/BF02664902.
- [54] A.K.S.K. Kumar, Criteria for predicting metallurgical instabilities in processing, M. Sc.(Eng) Thesis, Indian Inst. Sci. Bangalore, India. (1987).
- [55] Y. Prasad, Recent advances in the science of mechanical processing, *Indian J. Technol.* 28 (1990) 435–451.
- [56] S.I. Oh, Finite element analysis of metal forming processes with arbitrarily shaped dies, *Int. J. Mech. Sci.* 24 (1982) 479–493. doi:10.1016/0020-7403(82)90058-3.
- [57] C.H. Lee, S. Kobayashi, New solutions to rigid-plastic deformation problems using a matrix method, *Trans. ASME J. Engng Indust.* 95 (1973) 865–873.
- [58] P.E. Wellstead, *Introduction to Physical System Modelling*, 1979.
- [59] H. Ziegler, *Progress in Solid Mechanics*, ed. IN Sneddon and R. Hill, Amsterdam, Netherlands North-Holl. Publ. Co. 4 (1963) 93.
- [60] N. Srinivasan, Y.V.R.K. Prasad, P. Rama Rao, Hot deformation behaviour of Mg-3Al alloy—A study using processing map, *Mater. Sci. Eng. A.* 476 (2008) 146–156. doi:10.1016/j.msea.2007.04.103.
- [61] S. Venugopal, P. V Sivaprasad, A Journey With Prasad ' s Processing Maps, *J. Mater. Eng. Perform.* 12 (2003) 674–686.
- [62] G.E. Dieter, Evaluation of Workability for Bulk Forming Processes, in: *Metalwork. Bulk Form.*, ASM International,

- 2005: pp. 587–614. doi:10.31399/asm.hb.v14a.a0004017.
- [63] G.E. Dieter, H.A. Kuhn, S.L. Semiatin, *Handbook of Workability and Process Design*, 2003. doi:10.1361/hwprd2003p232.
- [64] R. Raj, Development of a Processing Map for Use in Warm-Forming and Hot-Forming Processes, *Metall. Trans. A*. 12 (1981) 1089–1097. doi:10.1007/BF02643490.
- [65] S.L. Semiatin, G.D. Lahoti, The occurrence of shear bands in isothermal, hot forging, *Metall. Trans. A*. 13 (1982) 275–288. doi:10.1007/BF02643318.
- [66] S.L. Semiatin, G.D. Lahoti, Deformation and unstable flow in hot forging of Ti-6Al-2Sn-4Zr-2Mo-0.1Si, *Metall. Trans. A*. 12 (1981) 1705–1717. doi:10.1007/BF02643754.
- [67] S.V.S.N. Murty, B.N. Rao, On the development of instability criteria during hotworking with reference to IN 718, *Mater. Sci. Eng. A*. 254 (1998) 76–82. doi:10.1016/S0921-5093(98)00764-3.
- [68] C. Poletti, J. Six, M. Hochegger, H.P. Degischer, S. Ilie, Hot deformation behaviour of low alloy steel, *Steel Res. Int.* 82 (2011) 710–718. doi:10.1002/srin.201000276.
- [69] F. Montheillet, J.J. Jonas, K.W. Neale, Modeling of dynamic material behavior: a critical evaluation of the dissipator power co-content approach, *Metall. Mater. Trans. A*. 27 (1996) 232–235. doi:10.1007/BF02647764.
- [70] S. Ghosh, Interpretation of microstructural evolution using dynamic materials modeling, *Metall. Mater. Trans. A*. 31 (2000) 2973–2974.
- [71] Y.-J. Qin, Q.-L. Pan, Y.-B. He, W.-B. Li, X.-Y. Liu, X. Fan, Modeling of flow stress for magnesium alloy during hot deformation, *Mater. Sci. Eng. A*. 527 (2010) 2790–2797. doi:DOI: 10.1016/j.msea.2010.01.035.
- [72] Y.V.R.K. Prasad, K.P. Rao, Effect of crystallographic texture on the kinetics of hot deformation of rolled Mg-3Al-1Zn alloy plate, *Mater. Sci. Eng. A*. 432 (2006) 170–177. doi:10.1016/j.msea.2006.05.159.
- [73] Y.C. Lin, M.-S. Chen, J. Zhong, Constitutive modeling for elevated temperature flow behavior of 42CrMo steel, *Comput. Mater. Sci.* 42 (2008) 470–477. doi:10.1016/j.commatsci.2007.08.011.
- [74] H.R.R. Ashtiani, P. Shahsavari, Strain-dependent constitutive equations to predict high temperature flow behavior of AA2030 aluminum alloy, *Mech. Mater.* 100 (2016) 209–218. doi:10.1016/j.mechmat.2016.06.018.
- [75] H. McQueen, N. Ryan, Constitutive analysis in hot working, *Mater. Sci. Eng. A*. 322 (2002) 43–63. doi:10.1016/S0921-5093(01)01117-0.
- [76] Y. Prasad, K.P. Rao, S. Sasidhar, *Hot working guide: a compendium of processing maps*, ASM international, 2015.
- [77] J. Bohlen, M.R. Nürnberg, J.W. Senn, D. Letzig, S.R. Agnew, The texture and anisotropy of magnesium-zinc-rare earth alloy sheets, *Acta Mater.* 55 (2007) 2101–2112. doi:10.1016/j.actamat.2006.11.013.
- [78] S.R. Agnew, M.H. Yoo, C.N. Tomé, Application of texture simulation to understanding mechanical behavior of Mg and solid solution alloys containing Li or Y, *Acta Mater.* 49 (2001) 4277–4289. doi:10.1016/S1359-6454(01)00297-X.
- [79] T. Mayama, M. Noda, R. Chiba, M. Kuroda, Crystal plasticity analysis of texture development in magnesium alloy during extrusion, *Int. J. Plast.* 27 (2011) 1916–1935. doi:10.1016/j.ijplas.2011.02.007.
- [80] S.E. Ion, F.J. Humphreys, S.H. White, Dynamic recrystallisation and the development of microstructure during the high temperature deformation of magnesium, *Acta Metall.* 30 (1982) 1909–1919. doi:10.1016/0001-6160(82)90031-1.
- [81] M.R. Barnett, A. Sullivan, N. Stanford, N. Ross, A. Beer, Texture selection mechanisms in uniaxially extruded magnesium alloys, *Scr. Mater.* 63 (2010) 721–724. doi:10.1016/j.scriptamat.2010.01.018.